

Advances in the Detection of As in Environmental Samples Using Low Energy X-ray Fluorescence in a Scanning Transmission X-ray Microscope: Arsenic Immobilization by an Fe(II)-Oxidizing Freshwater Bacteria

A. P. Hitchcock,[†] M. Obst,[‡] J. Wang,[§] Y. S. Lu,[§] and T. Tylliszczak^{*,||}

[†]Department of Chemistry and Chemical Biology, McMaster University, Hamilton, ON, Canada L8S 4M1

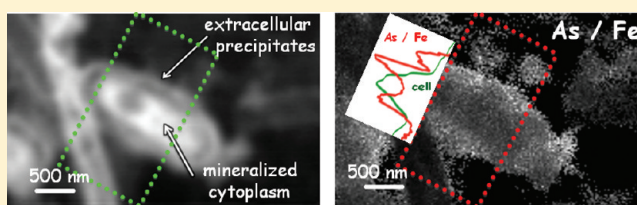
[‡]Center for Applied Geoscience, Eberhard Karls University Tuebingen, Tuebingen, Germany D-72076

[§]Canadian Light Source Inc., University of Saskatchewan, Saskatoon, SK, Canada S7N 0X4

^{||}Advanced Light Source, Lawrence Berkeley National Laboratory, Berkeley, California 94720, United States

Supporting Information

ABSTRACT: Speciation and quantitative mapping of elements, organic and inorganic compounds, and mineral phases in environmental samples at high spatial resolution is needed in many areas of geobiochemistry and environmental science. Scanning transmission X-ray microscopes (STXMs) provide a focused beam which can interrogate samples at a fine spatial scale. Quantitative chemical information can be extracted using the transmitted and energy-resolved X-ray fluorescence channels simultaneously. Here we compare the relative merits of transmission and low-energy X-ray fluorescence detection of X-ray absorption for speciation and quantitative analysis of the spatial distribution of arsenic(V) within cell-mineral aggregates formed by *Acidovorax* sp. strain BoFeN1, an anaerobic nitrate-reducing Fe(II)-oxidizing β -proteobacteria isolated from the sediments of Lake Constance. This species is noted to be highly tolerant to high levels of As(V). Related, As-tolerant *Acidovorax*-strains have been found in As-contaminated groundwater wells in Bangladesh and Cambodia wherein they might influence the mobility of As by providing sorption sites which might have different properties as compared to chemically formed Fe-minerals. In addition to demonstrating the lower detection limits that are achieved with X-ray fluorescence relative to transmission detection in STXM, this study helps to gain insights into the mechanisms of As immobilization by biogenic Fe-mineral formation and to further the understanding of As-resistance of anaerobic Fe(II)-oxidizing bacteria.



INTRODUCTION

X-ray excited X-ray fluorescence microprobe^{1,2} is a well established synchrotron-based, hard X-ray technique, which has been shown to have significant advantages with respect to both selectivity (tuning the incident energy to minimize interferences) and lower detection limits as compared to competing microanalysis methods such as electron microprobe X-ray fluorescence spectrometry,³ proton impact X-ray emission (PIXE),⁴ or energy dispersive X-ray (EDX) spectrometry in scanning or transmission X-ray microscopes.⁵ Whereas the detection limits are impressive, the spatial resolution in most hard X-ray microprobes is of the order of a micrometer or more, although some modern, zoneplate-based hard X-ray microscopes have been used to study trace elements in microbiological samples at a spatial resolution as good as 100 nm.⁶

Recently Kaulich and co-workers have implemented low-energy X-ray fluorescence (LE-XRF) detection with an annular arrangement of 8 silicon drift detectors (SDD) in a soft X-ray scanning transmission X-ray microscope (STXM) at the Elettra synchrotron and shown it to be an effective tool for

simultaneous multielement mapping in a range of samples.^{7–10}

The advantage of a soft X-ray rather than a hard X-ray STXM microprobe is that the spatial resolution is much higher, with routine operation at 25 nm¹¹ and a record spatial resolution of 10 nm.¹² Here we explore the use of single SDDs in STXMs at the Advanced Light Source (ALS) and at the Canadian Light Source (CLS) for studies of *Acidovorax* sp. strain BoFeN1 freshwater Fe(II)-oxidizing bacteria cultured with 1 mM levels of As(V). We show that the X-ray fluorescence detection channel provides a significantly lower detection limit relative to conventional transmission detection. Further, we have implemented X-ray fluorescence detection of X-ray absorption spectromicroscopy (near edge X-ray absorption fine structure (NEXAFS) image sequences or stacks¹³) which allows measurement of the NEXAFS signal from minor species, thus enabling chemical speciation as well as elemental mapping. A

Received: July 3, 2011

Revised: November 17, 2011

Accepted: January 27, 2012

Published: January 27, 2012

conference paper illustrating early results from this work has been presented.¹⁴

Ground and drinking water contamination with arsenic is a current environmental problem which affects human health in Southeast Asia,^{15–17} as well as the United States.¹⁸ The two common redox states of As are arsenite (As(III)) and arsenate (As(V)). The redox state and resulting differences in sorption to and coprecipitation of As within Fe-(oxy)hydroxides, the most efficient phases in immobilizing As in the environment, determine the toxicity, the mobility, and the environmental fate of As. Fe(II)-oxidizing bacteria have recently been identified as a possible factor in As immobilization.¹⁹ Such mechanisms would be of high environmental relevance since As-tolerant Fe-oxidizing *Acidovorax* strains have been found in groundwater wells in Bangladesh²⁰ and Cambodia.²¹ In this study we used *Acidovorax* sp. strain BoFeN1, isolated from the sediments of Lake Constance,²² which is known to oxidize iron and to form iron oxide precipitates first in the periplasm and later outside the cells in proximity to the outer membrane.^{23,24} Surprisingly, the growth of strain BoFeN1 is not affected by As concentrations as high as 500 μM ^{19,25} or 1 mM (this study). To date, neither the mechanisms of As-immobilization nor the detoxification mechanisms of this strain are fully understood.

Arsenate can be taken up into the periplasm through porins and is usually transported into the cytoplasm via phosphate uptake mechanisms that are usually not specific enough to distinguish between arsenate and phosphate. Once in the cytoplasm, arsenate is toxic and competes with phosphate for bonding sites. Classical arsenate detoxification mechanisms involve two essential steps: (1) reduction of arsenate to the more toxic form arsenite by an arsenate reductase, and (2) active transport from the cytoplasm into the periplasm by an arsenite efflux pump.^{26,27} Interestingly, arsenite formation was not observed when *Acidovorax* sp. strain BoFeN1 was incubated in the presence of arsenate and in the absence of dissolved iron,¹⁹ indicating that the classical detoxification mechanism might be of minor importance for this strain. To further our understanding we sought to determine whether or not arsenic is sorbed or coprecipitated in the Fe-oxides in the periplasm, and, if present, in which form. If As(III) is found associated with the Fe-minerals in the periplasm, this indicates BoFeN1 has a classical detoxification mechanism, but the diffusion of arsenite from the periplasm through the outer membrane is eventually hindered by the Fe-mineral precipitates. If As(V) is found at lower concentrations as compared to extracellular precipitates this might indicate that the outer membrane porins responsible for the arsenate uptake into the periplasm are down regulated. If As(V) is found at similar concentrations as compared to extracellular Fe-minerals, the BoFeN1 might have a specific phosphate uptake mechanism which efficiently prevents As(V) from entering the cytoplasm. If As(V) is enriched in the precipitates in the periplasm, this would suggest detoxification might occur by a yet unknown, specific arsenate transport mechanism(s) from the cytoplasm into the periplasm. Spatially highly resolved (<50 nm) chemical speciation mapping is required to solve this question. Although soft X-ray STXM has a suitable spatial resolution, the standard transmission detection does not have the sensitivity to detect and speciate As at the relevant local concentrations. Here we have combined the sensitivity of LE-XRF detection with the spectromicroscopic capabilities of modern soft X-ray STXM beamlines in order to investigate this interesting and uncharted question.

Additionally, measuring the relative sorption/coprecipitation capacity of extra- and intracellularly formed biogenic vs abiotically formed Fe-minerals could provide valuable information for optimizing remediation strategies for contaminated wells or filter systems used for water remediation. A high potential of nitrate-reducing, Fe(II)-oxidizing bacteria to mediate efficient removal of arsenic from contaminated waters has been postulated.^{28,29} Our study intends to better understand the mechanisms involved in bonding As in such systems, which might help optimize bioremediation strategies, for example by changing geochemical conditions to influence growth or activity of microbial communities, in order to maximize the stability of As-bonding.

■ EXPERIMENTAL SECTION

A compact Peltier-cooled SDD system (Amptek model X-123SDD, 7 mm² active area) was installed in the STXM at ALS beamline 11.0.2 with the detector sufficiently close to the sample to obtain a large solid angle (estimated to be 0.5 sr) (see Supporting Information Figure S-1a). The windowless detector was operated at a pressure of 1×10^{-5} Torr. For some measurements an aluminized silicon nitride membrane was used to reduce interference by scattered light from the HeNe laser used for interferometric positional control.³⁰ We ultimately found that an aluminum metal collimator (1.5 mm diameter aperture) combined with careful positioning of the XRF detector relative to the order sorting aperture (OSA) and the sample support was sufficient to eliminate background signals from both the laser and X-rays scattered/emitted from the OSA. The detector was mounted orthogonal to the X-ray beam. The elliptically polarizing undulator (EPU) was adjusted so that the E-vector of the incident light pointed directly at the SDD, to minimize Rayleigh scattering.³¹ When the E-vector was intentionally oriented orthogonal to the SDD the Rayleigh scattering signal was found to be similar in magnitude to, or larger than, the strongest X-ray fluorescence from the sample (SI Figure S-1b). We confirmed that the elastic scattering signal made negligible contribution to the results, even when using incident photon energies within the energy width of the As $L\alpha$ XRF peak (see SI Figure S-2).

The CLS system was similar except that the SDD was from XGLab,⁸ and is a sealed unit with a polymer membrane window. The active area of the XGLab SDD is 30 mm² versus 7 mm² for the Amptek detector. The bulky support structure for the CLS SDD detector prevented positioning the SDD as close as at the ALS, and thus, while higher signal rates were achieved at the CLS, the gain in signal was ~ 2 , rather than >4 expected from the relative areas of the SDDs.

The samples were chemo-organo-trophic, nitrate-reducing β -proteobacteria of the strain BoFeN1 that is closely related to *Acidovorax* sp. and grows mixotrophically oxidizing Fe(II) and using acetate as the organic cosubstrate.²² The cells were grown anaerobically in freshwater culture medium containing 10 mM NaNO₃ and 5 mM Na-acetate and 1 mM of phosphate as described previously.²⁵ Fifteen mM Fe(II) from a sterile FeCl₂ stock solution was added, followed by the precipitation of whitish Fe(II)-carbonate and -phosphate minerals. The medium was filtered prior to use to exclude abiotically formed minerals, resulting in dissolved Fe(II) concentrations of ~ 6 mM and a dissolved phosphate concentration of ~ 20 μM . Arsenate was added to the culture medium at a concentration of 1 mM for sorption/coprecipitation experiments prior to inoculation with 5% of a acetate/nitrate grown culture. For

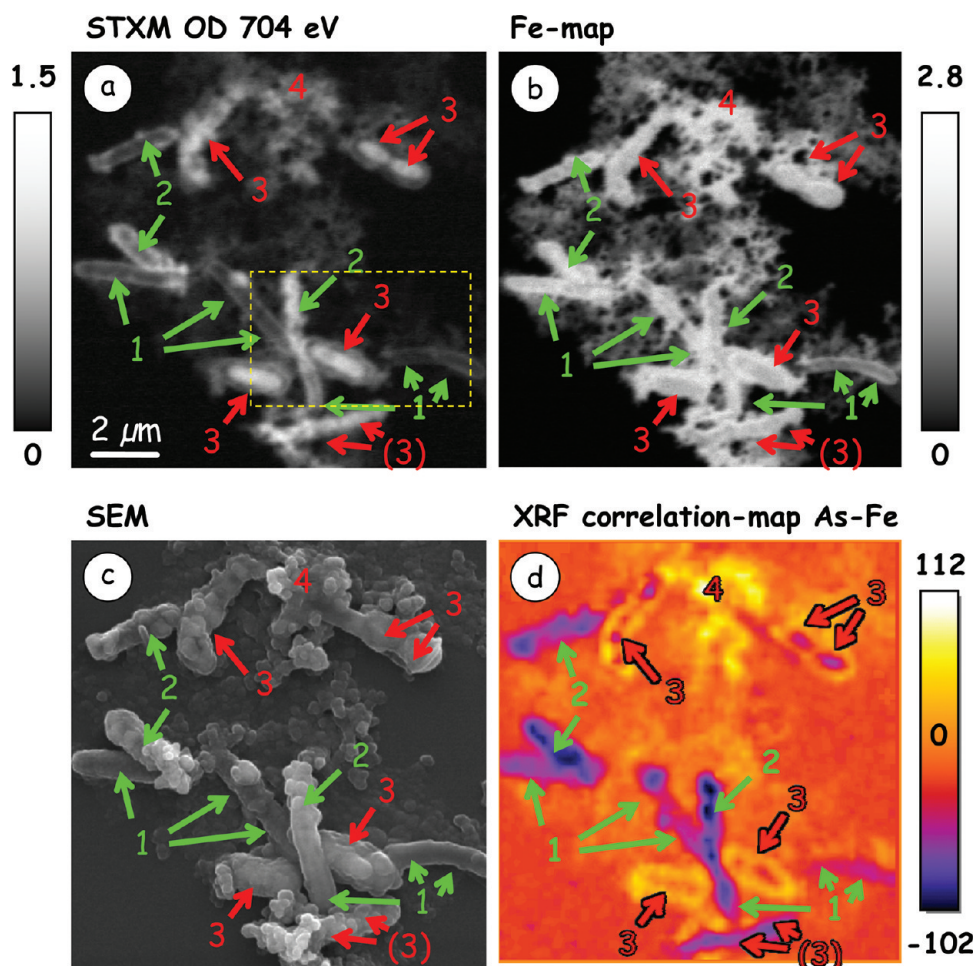


Figure 1. (a) (Area A) STXM optical density (OD) image of a *Acidovorax* sp. strain BoFeN1 sample recorded with transmission detection at 704 eV (30 nm pixels, 1 ms/pixel). The dashed rectangle indicates the area examined in more detail in Figure 5. (b) Fe map from difference of STXM OD images at 709.8 eV (Fe(III) L_3 absorption maximum) and 704 eV. (ALS). The gray scale indicates the OD range. (c) Scanning electron microscope (SEM) image of the same area, recorded with a Tescan Vega-II SBU using 20 kV beam energy and a working distance of 6 mm. The sample was lightly carbon-coated to reduce charging. (d) Correlation map of As and Fe calculated from XRF maps of As and Fe using the Image CorrelationJ plugin for Fiji (see text for details).

details see ref 19. The cells were harvested after 1 week of growth when the Fe(II) was completely oxidized and the As-concentration remaining in the medium was $69 \mu\text{M}$ as determined by ICP-MS. The harvested cells were centrifuged and washed twice with deionized water to remove salts. A few microliters of the culture were placed on an X-ray transparent Si_3N_4 membrane (Norcada Inc.) and then air-dried.

X-ray fluorescence spectra and maps using photon energies as high as 1700 eV, well above the As 2p edge, and X-ray fluorescence detected NEXAFS image sequences in the As 2p absorption were measured. Analysis was performed using aXis2000.³² The sample was suitable for transmission measurements and was sufficiently thin that corrections for self-absorption were not required for higher-energy XRF signals. In some XRF maps of low-Z components shadowing was observed, indicating self-absorption of the emitted X-rays for the geometry used. Correlation maps were calculated from the XRF element maps of As and Fe using the Image CorrelationJ plugin³³ for Fiji.³⁴

RESULTS

Figure 1a shows a STXM image (after conversion to optical density, OD) of a region of the *Acidovorax* sp. strain BoFeN1

sample (area A) recorded with transmission detection at 704 eV just below the Fe 2p edge, while Figure 1b shows an Fe map, the difference of STXM OD images at 704 and 709.8 eV (Fe(III) L_3 peak). This region of the sample contains a number of BoFeN1 cells at different individual stages of encrustation in Fe-minerals that are the result of oxidation of Fe(II) by the bacteria. An image sequence at the C 1s edge recorded by transmission detection is presented and analyzed in SI Figures S-3 and S-4 to provide the biochemical background. Figure 1c presents an SEM image of the same area. The SEM image has higher spatial resolution and shows fine surface details, whereas the STXM image shows the cells at the interior of the Fe oxide biomineral deposits. There appear to be three stages of cell encrustation: (1) The first type of cells (labeled 1 in Figure 1) have a rather clean surface with none or very few extracellular precipitates (Figure 1c). However, these cells have a dense “rim” in the X-ray absorption image, which is caused by the precipitation of a thin (40 nm) layer of Fe-minerals in the periplasm (visible in X-ray transmission at 704 eV, Figure 1a). (2) The second type of cells (labeled 2) have some precipitates closely associated with their cell surface. These precipitates have a cauliflower like appearance in SEM images (Figure 1c) and are not particularly dense (Figure 1b). (3) The third type

of cells (labeled 3) are encrusted in a thick layer of Fe-minerals (Figure 1b and c). In contrast to the second type of cells, the former cytoplasm of type 3 cells is filled with dense Fe-minerals (Figure 1a and b).

The stage of encrustation seems to have a systematic influence on the As-bonding, which is shown in the correlation map of Fe and As in Figure 1d. The As/Fe ratio was depleted in the insides of the cells, independent of the stage of precipitation (i.e., for cells with an intact cytoplasm (stages 1 and 2), and for cells filled with Fe-minerals (stage 3). This is indicated in the correlation map by the dark colors within the cells as compared to their surroundings. However, only cells at stage 3 (i.e., cells with internal precipitates) had a wide rim of extracellular precipitates that were enriched in As, as indicated by the bright colors in Figure 1d. Additionally, some precipitates were equally rich in As, but seemed not to be associated with bacterial cells.⁴

A STXM image of a different region of the same sample (area B) recorded with transmission detection at 1342 eV is shown in Figure 2a. X-ray fluorescence spectra (Figure 2b) were recorded with an incident beam of 5×10^8 ph/s in a sub-50 nm spot centered on an As hot spot (white circle in Figure 2a) at two incident photon energies—1315 eV, above the onset of the Mg 1s edge, and 1340 eV, above the As 2p edge. The XRF spectra show strong signals from O $K\alpha$, Fe $L\alpha$, a weak Na $K\alpha$ signal, and a peak at ~ 1.3 keV which, as subsequent XRF-yield spectromicroscopy showed, is a composite of signals from the As $L\alpha$ line at 1.28 keV and the Mg $K\alpha$ line at 1.25 keV. The difference in intensity of the Fe peak in the two XRF spectra probably reflects spatially highly variable concentrations (iron is known to be concentrated in the periplasm of the cells, i.e., between the inner and outer membrane of the bacteria^{23,24}), combined with small shifts in the position of the incident X-ray beam. A sequence of images (XRF-yield stack) was recorded from 1308 to 1356 eV, covering the Mg 1s and As 2p edges while simultaneously recording the transmitted X-rays and the full XRF spectrum at each pixel. Figure 2c shows the absorption spectrum of the hot spot extracted from the transmission signal and converted to OD using the I₀ signal from the Si₃N₄ window, far from the bacteria and deposits. The NEXAFS spectrum recorded with transmission detection (blue curve in Figure 2c) is featureless at the Mg 1s or As 2p edges. However, when the X-ray fluorescence yield signal from the combined Mg $K\alpha$ and As $L\alpha$ lines was extracted from the XRF spectra at the region of the hot spot, very clear Mg 1s and As 2p NEXAFS spectral features were observed, with the NEXAFS spectra reflecting the oxidation states and the chemical environment of these elements. The shape of the As 2p spectrum is very similar to that reported for an amorphous As(V)–Fe(III) phase,³⁵ and thus As is predominantly in the As(V) arsenate state. The Mg is in the Mg(II) oxidation state, as indicated by comparison to the spectra of a Mg(II)-containing clay reported by Tran et al.³⁶ Figure 2c is unambiguous evidence of a significantly lower detection limit for energy-resolved X-ray fluorescence relative to transmission detection. We estimate there is more than an order of magnitude improvement in the detection limit. Quantitation of the XRF signal is being carefully evaluated and will be reported elsewhere. There is a shift of 24(S) eV in the peak position of the overlapping Mg $K\alpha$ /As $L\alpha$ XRF signals, when changing from an incident energy of 1315 to 1340 eV (Figure 2b). This shift is consistent with the known energy shift of 26 eV between these two X-ray emission lines—Mg $K\alpha$ at 1254 eV, and As $L\alpha$ at 1282 eV). It occurs because

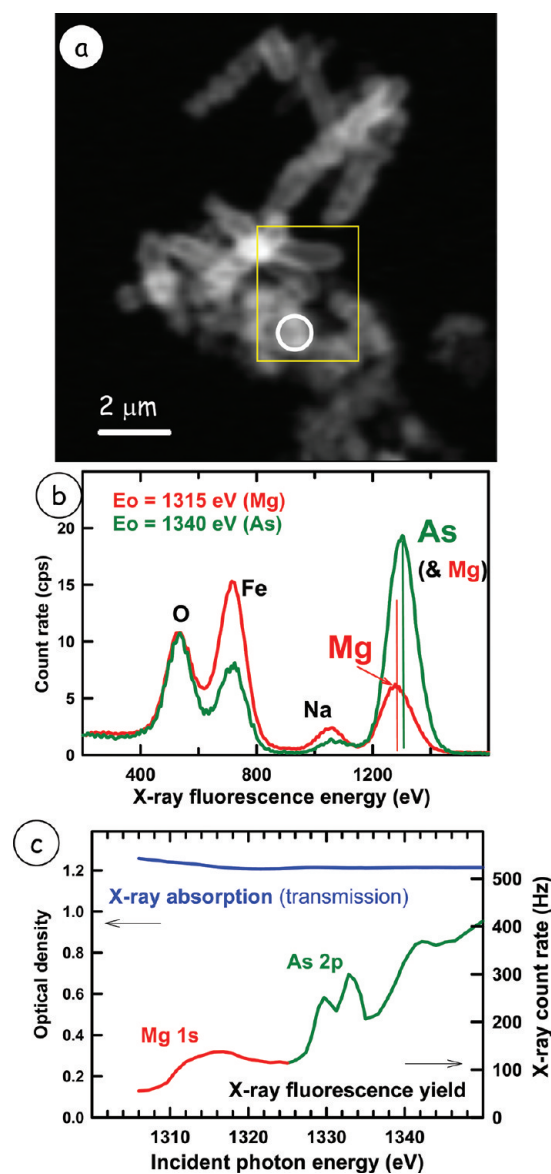


Figure 2. (a) (Area B) STXM absorption image recorded using 1342 eV photon energy with 1 ms/pixel from the BoFeN1 sample. Circle = location of the spot XRF spectrum presented in (b). The rectangle indicates the area examined by XRF-mapping in Figure 3. (b) X-ray fluorescence spectra (600 s), recorded with Amptek SDD with 1315 and 1340 eV incident energy. (c) X-ray absorption signal (blue) from the hot spot extracted from transmission signal (blue) compared to the overlapping Mg $K\alpha$ and As $L\alpha$ XRF-yield signal extracted from the same point. Both spectra were extracted from a simultaneous transmission and XRF-yield image sequence (1308–1356 eV, 63 incident photon energies, 180 ms dwell per pixel). (ALS).

only Mg $K\alpha$ can be emitted when the incident photon energy is 1315 eV (below the onset of the As 2p edge) whereas the more abundant As $L\alpha$ dominates the overall signal when the incident photon energy is 1340 eV, where the As 2p absorption is strong. It is possible, but probably not practical, to use this small shift to map the minor Mg component, by careful curve fitting of the XRF spectrum. However it is much simpler and more powerful to use the XRF-yield absorption spectra (Figure 2c) to speciate, and map the Mg and As separately. The NEXAFS-derived Mg and As maps of this area were presented earlier (see Figure 3 in ref 14). In the case of the area examined

in Figure 2 of this manuscript, the Mg and As spatial distributions were similar, with a relative signal level (Mg/As) of 10–20%.

Elemental mapping can be done at an incident photon energy well above the thresholds for core excitation of edges of interest and recording X-ray fluorescence spectra for an appropriate dwell at each pixel, over an array of pixels. Figure 3a shows the XRF spectrum averaged over a region of a cell and

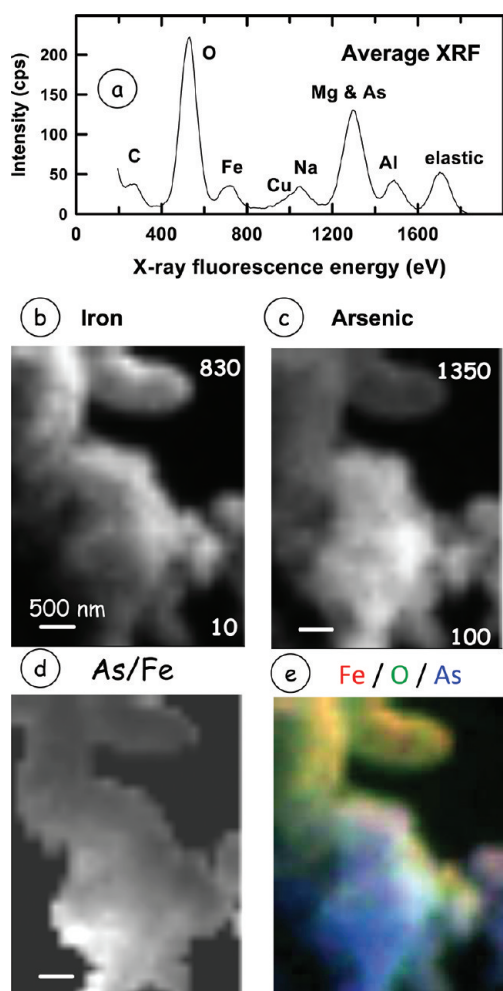


Figure 3. (a) X-ray fluorescence spectrum, recorded with an XGLab SDD, averaged over all pixels of an X-ray fluorescence map (1700 eV, 6 s/pixel, 40×33 pixels) in a subset of area B. (b) Fe map, (c) As (and some Mg) map from integration of the appropriate XRF peaks (1360 eV, 2.6 s/pixel, 27×34 pixels). The numbers indicate the minimum and maximum counts in each map. Maps of all other elements recorded in the same measurement are presented in the Supporting Information. (d) Ratio of As to Fe map, with a masking on the total XRF map to remove areas with negligible signal. (e) Rescaled color-coded composite of the Fe $L\alpha$ (red), O $K\alpha$ (green), and As $L\alpha$ (blue) maps. (CLS).

associated Fe-minerals of the *Acidovorax* sp. strain BoFeN1 sample recorded using 1700 eV incident photon energy (Figure 3 is a subset of area B, indicated by the yellow rectangle in Figure 2a). At this energy there is complete separation between the relatively small elastic scattering peak at 1700 eV and the X-ray fluorescence signal. To obtain better statistics we chose to measure XRF maps with an incident photon energy of 1360 eV, closer to the peak of the As 2p absorption cross-section. Figure

3b and c are XRF maps for iron and arsenic (the As signal also includes up to ~10% Mg signal, see Figure 2c). The XRF-derived maps for the other elements are presented in Supporting Information (Figure S-5). Figure 3d presents the ratio of the As and Fe signals from the maps in Figure 3b,c. In this case the relative amount of As compared to Fe is greatest in the densely packed agglomerate of encrusted cells, extracellular precipitates, and extracellular organic material in the lower center of the map. In contrast, relatively lower As/Fe ratios were observed in the distinct, nonencrusted cell seen at the top of the imaged area. Figure 3e is a color coded composite of the As, O, and Fe maps.

Figure 4 presents NEXAFS spectra at the As 2p edge extracted from an XRF-yield image sequence recorded in area A

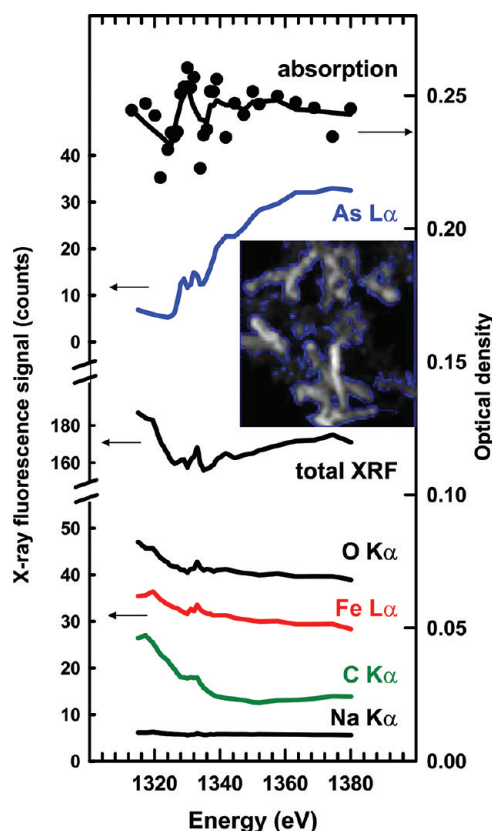


Figure 4. Spectra of the cellular regions in the As 2p region (1315–1380 eV) derived from transmission (OD) and energy resolved XRF-yield for the As $L\alpha$, C $K\alpha$, N $K\alpha$, O $K\alpha$, Fe $L\alpha$, and Na $K\alpha$ signals. The insert image shows the *Acidovorax* sp. strain BoFeN1 sample (area A). The transmission-derived absorption and XRF-yield signals are the average of all pixels in the cellular regions (inside of the blue lines). (ALS).

(same as Figure 1). The insert map shows the region of the sample from which these spectra were obtained, which is the area of all cells, inside the blue lines. The yield of the As $L\alpha$ peak in the XRF spectrum (integrated from 1210 to 1360 eV) shows a very high quality As 2p spectrum, which has a shape similar to that reported for an amorphous As(V)–Fe(III) phase,³⁵ as also seen in Figure 2c. The signal below the onset of the As 2p excitation is very low, indicating very little Mg 1s signal. The shape of the As 2p spectrum is identical in all regions (on/off cells) (see SI Figure S-6) indicating only As(V) is present. The yield curves for other elements show a declining

signal, as expected. There is a small structure at the As 2p edge in the total XRF yield as well as in the yield signals of the non-As elements whose origin is not understood. The OD spectrum derived from the transmission signal, recorded at the same time as the XRF-yield NEXAFS image sequence, does not show the As 2p spectrum, clearly showing the much lower detection limits that are provided by using energy selective XRF detection of the NEXAFS signal. SI Figure S-7 and associated text presents a direct comparison of these STXM-XRF results with those from the identical area recorded using energy-dispersive X-ray fluorescence in a scanning electron microscope (SEM-EDX).

Figure 5 shows a detailed STXM-XRF analysis of the area indicated by the dashed rectangle in Figure 1a). In addition to the OD image from transmission (Figure 5a), Figure 5 presents

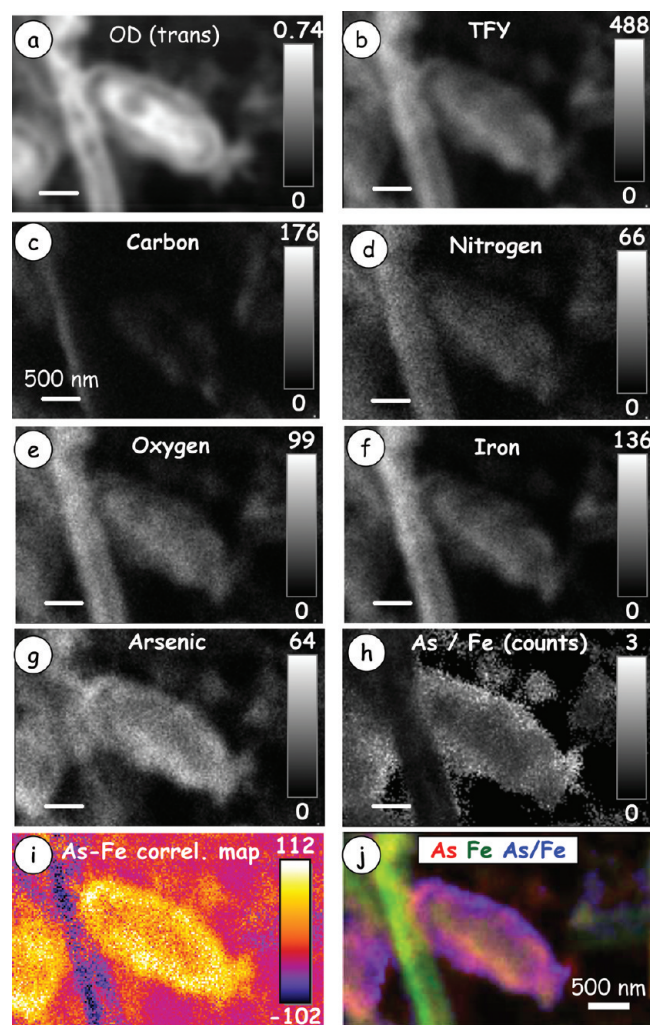


Figure 5. (subset of area A) (a) OD image derived from the transmission signal. (b) Total fluorescent yield (0.4 s/pixel, 176×112 pixels). (c–g) XRF elemental maps of the indicated elements recorded with $E_0 = 1346$ eV. (h) Ratio of the As to the Fe map. The raw ratio was multiplied by a mask derived by thresholding both As and Fe maps (>5 cts) to remove artifacts from regions with very low signal. (i) Correlation map of As and Fe calculated from the maps (g) and (f) using the Image CorrelationJ plugin for Fiji; see text for details. (j) Rescaled color composite of the As (red), Fe (green), and As/Fe-ratio (blue) maps. See Supporting Information for further analysis of these results. (ALS).

total fluorescence yield (b), and elemental maps (c–g). The arsenic (Figure 5g) is strongly affiliated with the extracellular precipitates of a fully encrusted and mineral-filled cell (type 3 cell), with relatively low internal As/Fe ratios (i) and enhanced levels at the outer surfaces. The linear grayscale ratio map of As/Fe (h) was calculated from the STXM XRF maps (g) and (f), respectively. The raw ratio was multiplied by a mask derived from threshold levels of 5 or more counts per pixel for both maps (Figure 5g, h) to exclude artifacts from regions with low or zero signal. Figure 5i shows a correlation map calculated from the As (g) and Fe (f) maps. The correlation map clearly shows enhanced levels of As relative to Fe in the extracellular precipitates of the fully encrusted and Fe-mineral filled cell. The periplasmic Fe-mineral precipitates of cells at an early (individual) stage of precipitation (i.e., cells without extracellular encrustation, type 1 cells), such as the vertical cells on the left side or the cells on the right (barely visible in the XRF maps, compare Figure 1c) are depleted in their As/Fe ratios. Figure 5j, an RGB overlay of As (red), Fe (green), and the As/Fe ratio (blue), again highlights that the As(V) is not homogeneously distributed within the Fe-oxides and that there is a strong enhancement of As relative to Fe at the outer surface of the extracellular precipitates of type 3 cells. The average count ratios of As/Fe are 0.77 for the area of the cytoplasm, 1.09 for the inner half of the extracellular precipitates, and 1.46 for the outer half of the extracellular precipitates associated with the cell in the center of Figure 5. Histograms showing the ratios of the respective areas are presented in SI Figure S-8 while an average profile of the As/Fe ratios across the cell is presented in SI Figure S-9.

DISCUSSION

These results show that low-energy XRF detection in a soft X-ray STXM is a viable technique, as previously demonstrated by Kaulich and co-workers at Elettra,^{7–10,39} despite the very low fluorescence yields and the low flux compared to hard X-ray or spectroscopy-only implementations. For the first time we have provided clear proof that LE-XRF yield provides lower detection limits than transmission detection (see Figures 2 and 4). However, does STXM-XRF provide gains relative to other elemental mapping methods? Comparison of Figures S-7a and S-7c indicates the spatial resolution of SEM-EDX mapping is limited relative to XRF mapping in a soft X-ray scanning transmission X-ray microscope. This can be explained by the rather large interaction volume of a 20-kV electron beam interacting with the specimen. The diameter of the interaction volume was estimated to be in the range of several μm using the Casino Monte Carlo simulation package.⁴⁰ Additionally, the nonideal shape of the nonflat sample surface might allow secondary electrons to escape from the spot excited by the primary beam which can then excite adjacent regions of the sample, which will further reduce spatial resolution. In contrast, the spatial resolution in the STXM-XRF maps does allow for identification of features in the size range of 100 nm or slightly below (see Figure 5). The spatial resolution in the XRF maps might be somewhat degraded from that expected for STXM with a 25-nm outer zone width zone plate since the exit slits of the beamline ($50 \mu\text{m} \times 50 \mu\text{m}$) were much wider than normal ($10 \mu\text{m} \times 10 \mu\text{m}$), which reduces coherent fraction and degrades spatial resolution. The increased incident flux (to $\sim 5 \times 10^8$ ph/s in the spot, relative to 2×10^7 ph/s in normal operation) and the relatively long counting time per pixel (120–180 ms), were necessary to obtain sufficient XRF signal

intensities. However, even with somewhat degraded spatial resolution, the results demonstrate identification of subcellular features in the sub-100 nm size range such as the Fe-mineral precipitates in the periplasm which have been studied extensively and shown to be 40 nm wide^{23,24} and appear as a rim around nonencrusted cells in the 2-d projection maps (e.g., vertical cell on the left of Figure 5). Taking into account the information of the previously mentioned TEM studies, such as the cell diameter and the dimensions of the periplasmic precipitates, the periplasmic precipitates can be identified confidently by STXM-XRF and differentiated from extracellular precipitates, when they appear on different cells. Periplasmic precipitates of extracellularly heavily encrusted cells are more difficult to identify (compare Figure 5a, b, e, and f). Of course the most useful attribute of STXM-XRF relative to SEM-EDX is the ability to vary the incident photon energy and thereby measure XRF-yield NEXAFS signals, which provides speciation capability.

Previous studies of anoxic Fe-oxidation by *Acidovorax* sp. strain BoFeN1 have shown that biogenic Fe(II) oxidation and precipitation starts in the periplasm of the cells.^{23,24} However, at different stages of precipitation both slightly and heavily encrusted cells can be found (see Figure 1a). This is consistent with a previous study,⁴¹ which simultaneously found a range of encrustation stages, from cells with a number of small globules of Fe-oxides attached to their surface, to cells that were fully enclosed in an envelope of Fe-oxides. The main Fe mineral phase formed by this strain is goethite, but recently carbonate green rust has been identified as a metastable, mixed valence (Fe(II), Fe(III)) transition phase at early stages of precipitation.⁴² In their study, Pantke et al.⁴² found that the green rust was not fully converted to goethite after several days of Fe(II) oxidation. In the presence of high concentrations of As(III) and As(V) minor amounts of ferrihydrite were also found to be precipitated. The spatial distribution of the different mineral phases, their association with the cells, and the resulting differences in As sorption/coprecipitation properties could not be studied so far since conventional transmission STXM could not detect the As except for one study with As levels in the few percent range.³⁵

Conventional detoxification mechanisms include two steps—the reduction of As(V) to As(III) in the cytoplasm and an active transport pump for As(III) from the cytoplasm into the periplasm. We did not find any spectroscopic evidence for As(III) and thus, reduction of As(V) to As(III) by BoFeN1. This is in keeping with previous results: As(III) formation was not observed when *Acidovorax* sp. strain BoFeN1 was incubated in presence of arsenate and in absence of dissolved iron.¹⁹ Thus, a classical detoxification mechanism does not explain the observed depletion of the As/Fe ratio in the cytoplasmic precipitates and would even be in contradiction with the low ratios that we found in periplasmic Fe-mineral precipitates of BoFeN1. Further studies are required to solve this open question.

There could be several reasons that the As/Fe ratios are enhanced in the extracellular precipitates of cells that are completely filled with Fe-minerals and therefore can no longer be metabolic active. When the cells are filled with minerals, likely the cytoplasmic membrane and finally the outer membrane become disrupted, resulting in a release of the cytoplasm. This results in a change of the chemical micro-environment of the cell such as a pH increase. Furthermore, the release of organic compounds might result in organic coatings

of the extracellular precipitates, or in changes in the mineral composition. Differences in the mineralogy of the periplasmic and extracellular precipitates cannot be excluded completely since the Fe L_{2,3} spectra are not very specific. The major phases identified in bulk samples by Moessbauer spectroscopy, EXAFS and XANES spectroscopy, and XRF were goethite, ferrihydrite, and, at early stages of oxidation, carbonate green rust.⁴² From abiotic studies it is known that pure goethite has a higher affinity for bonding arsenate as compared to ferrihydrite.⁴³ The influence of organic matter released by the cells however, is not yet clear. Recently, it has been shown that in presence of complexes of humic substances and Fe(III), large fractions of arsenate are bound in ternary humic-Fe(III)-As(V) complexes,⁴⁴ which suggests there could be a significant influence of the organic matter in As-bonding in cell-mineral aggregates of Fe(II)-oxidizing bacteria.

A more detailed study of the different stages of Fe-mineral precipitation by *Acidovorax* sp. strain BoFeN1 is necessary to compare the influence of the stage of culture growth and the related mineral precipitation on the sorption/coprecipitation behavior of arsenate on/within the biogenic minerals. Further comparisons of the As content of cell-external and cell-internal precipitates will help understand As-immobilization by these microorganisms. Detailed STXM-XRF results on individual cells which address these issues have been obtained and will be reported in a follow-up paper. Summarizing, low-energy X-ray fluorescence detection has been implemented in two interferometer controlled STXMs and shown to provide lower detection limits for As than conventional transmission detection. Arsenic in *Acidovorax* strain BoFeN1 was found to be associated primarily with the extracellular Fe-rich crust in intimate contact with the cellular membrane of more mature cells, but has relatively low affinity for young cells which have not produced major amounts of extracellular Fe oxide deposits.

■ ASSOCIATED CONTENT

📄 Supporting Information

Figures S1–S9. This material is available free of charge via the Internet at <http://pubs.acs.org>.

■ AUTHOR INFORMATION

Corresponding Author

*E-mail: aph@mcmaster.ca; phone: 905 525-9104, ext 24749.

■ ACKNOWLEDGMENTS

This work was supported by NSERC (Canada), Canada Foundation for Innovation and the Canada Research Chair program and by the Emmy-Noether program of the DFG to M.O. (OB 362/1-1). We thank Dr. Claudia Pantke and Petra Kühner for help with the cell cultivation, Nikolas Hageman for help with the chemical analysis, Drs. Andreas Kappler and Chad Saltikov for discussion and support. We also thank Drs. Burkhard Kaulich and Alessandra Gianoncelli (Elettra) for assistance with commissioning the XGLab detector and general advice on STXM-LEXRF. Furthermore, we thank two anonymous reviewers for their valuable comments on our first version of this paper. The Advanced Light Source is supported by the Director, Office of Energy Research, Office of Basic Energy Sciences, Materials Sciences Division of the U.S. Department of Energy, under Contract DE-AC02-05CH11231. The CLS is supported by NSERC, CIHR, NRC, the Province of Saskatchewan, WEDC, and the University of Saskatchewan.

REFERENCES

- (1) Manceau, A.; Marcus, M. A.; Tamura, M. Quantitative speciation of heavy metals in soils and sediments by synchrotron X-ray techniques. *Rev. Mineral. Geochem.* **2002**, *49*, 429–483.
- (2) Lanzirotti, A.; Tappero, R.; Schu, D. G. Practical Application of Synchrotron-Based Hard X-Ray Microprobes in Soil Sciences. *Dev. Soil Sci.* **2010**, *34*, 27–72.
- (3) Ro, C.-U.; Osán, J.; Van Grieken, R. Determination of low-Z elements in individual environmental particles using windowless EPMA. *Anal. Chem.* **1999**, *71*, 1521–1528.
- (4) Govil, I. M. Proton Induced X-ray Emission – A tool for non-destructive trace element analysis. *Curr. Sci.* **2001**, *80*, 1542–1549.
- (5) Goldstein, J. I.; Newbury, D.; Joy, D. C.; Lyman, C.; Echlin, P.; Lifshin, E.; Sawyer, L.; Michael, J. *Scanning Electron Microscopy and X-Ray Microanalysis*; Springer: New York, 2003; ISBN 0306472929.
- (6) Kemner, K. Hard X-ray micro(spectro)scopy: A powerful tool for the geomicrobiologists. *Geobiology* **2008**, *6*, 270–277.
- (7) Alberti, R.; Longoni, A.; Klatka, T.; Guazzoni, C.; Gianoncelli, A.; Bacescu, D.; Kaulich, B. A Low Energy X-Ray Fluorescence Spectrometer for Elemental Mapping X-Ray Microscopy. *IEEE Nucl. Sci. Symp. Conf. Rec.* **2008**, *N14*, 3–6.
- (8) Alberti, R.; Klatka, T.; Longoni, A.; Bacescu, D.; Marcello, A.; De Marco, A.; Gianoncelli, A.; Kaulich, B. Development of a low-energy x-ray fluorescence system with sub-micrometer spatial resolution. *X-ray Spectrom.* **2009**, *38*, 205–210.
- (9) Gianoncelli, A.; Klatka, T.; Alberti, R.; Bacescu, D.; De Marco, D.; Marcello, A.; Longoni, A.; Kaulich, B.; Kiskinova, M. Development of a low-energy X-ray fluorescence system combined with X-ray microscopy. *J. Phys. Conf. Ser.* **2009**, *186*, 012007–3.
- (10) Gianoncelli, A.; Kaulich, B.; Alberti, R.; Klatka, T.; Longoni, A.; De Marco, A.; Marcello, A.; Kiskinova, M. Simultaneous soft X-ray transmission and emission microscopy. *Nucl. Inst. Meth. A* **2009**, *608*, 195–199.
- (11) Ade, H.; Hitchcock, A. P. NEXAFS microscopy and resonant scattering: Composition and orientation probed in real and reciprocal space. *Polymer* **2008**, *49*, 643–675.
- (12) Chao, W.; Fischer, P.; Tylliszczak, T.; Reka, S.; Anderson, E.; Naulleau, P. Real Space Soft X-ray Imaging at 10 nm Spatial Resolution. *Phys. Rev. Lett.* **2011**, in review.
- (13) Jacobsen, C.; Wirick, S.; Flynn, G.; Zimba, C. Soft X-ray Spectroscopy from Image Sequences with Sub-100 nm Spatial Resolution. *J. Microsc.* **2000**, *197*, 173–184.
- (14) Hitchcock, A. P.; Tylliszczak, T.; Obst, M.; Swerhone, G. D. W.; Lawrence, J. R. Improving sensitivity in soft X-ray STXM using low energy X-ray fluorescence. *Microsc. Microanal.* **2010**, *16* (S-2), 924–925.
- (15) Smedley, P. L.; Kinniburgh, D. G. A review of the source, behaviour and distribution of arsenic in natural waters. *Appl. Geochem.* **2002**, *17*, 517–568.
- (16) McArthur, J. M.; Banerjee, D. M.; Hudson-Edwards, K. A.; Mishra, R.; Purohit, R.; Ravenscroft, P.; Cronin, A.; Howarth, R. J.; Chatterjee, A.; Talukder, T.; Lowry, D.; Houghton, S.; Chadha, D. K. Natural organic matter in sedimentary basins and its relation to arsenic in anoxic ground water: The example of West Bengal and its worldwide implications. *Appl. Geochem.* **2004**, *19*, 1255–1293.
- (17) Harvey, C. F.; Ashfaq, K. N.; Yu, W.; Badruzzaman, A. B. M.; Ashraf Ali, M.; Oates, P. M. H.; Michael, A.; Neumann, R. B.; Beckie, R.; Islam, S.; Ahmed, M. F. Groundwater dynamics and arsenic contamination in Bangladesh. *Chem. Geol.* **2006**, *228*, 112–136.
- (18) Schreiber, M. E.; Simo, J. A.; Freiberg, P. G. Stratigraphic and geochemical controls on naturally occurring groundwater, eastern Wisconsin, USA. *Hydrogeol. J.* **2000**, *8*, 161–176.
- (19) Hohmann, C.; Morin, G.; Ona-Nguema, G.; Guigner, J. M.; Brown, G. E.; Kappler, A. Molecular-level modes of As binding to Fe(III) (oxyhydr)oxides precipitated by the anaerobic nitrate-reducing Fe(II)-oxidizing Acidovorax sp. strain BoFeN1. *Geochim. Cosmochim. Acta* **2011**, No. 10.1016/j.gca.2011.02.044.
- (20) Sutton, N. B.; van der Kraan, G. M.; van Loosdrecht, M. C. M.; Muyzer, G.; Bruining, J.; Schotting, R. J. *Water Res.* **2009**, *43*, 1720–1730.
- (21) Lear, G.; Song, B.; Gault, A. G.; Polya, D. A.; Lloyd, J. R. Molecular Analysis of Arsenate-Reducing Bacteria within Cambodian Sediments following Amendment with Acetate. *Appl. Environ. Microbiol.* **2007**, *73*, 1041–1048.
- (22) Kappler, A.; Schink, B.; Newman, D. K. Fe(III) mineral formation and cell encrustation by the nitrate-dependent Fe(II)-oxidizer strain BoFeN1. *Geobiology* **2005**, *3*, 235–245.
- (23) Miot, J.; Benzerara, K.; Morin, G.; Kappler, A.; Bernard, S.; Obst, M.; Ferard, C.; Skouri-Panet, F.; Guigner, J. M.; Posth, N.; Galvez, M.; Brown, G. E. Jr.; Guyot, F. Iron biomineralization by anaerobic neutrophilic iron-oxidizing bacteria. *Geochim. Cosmochim. Acta* **2009**, *73*, 696–711.
- (24) Miot, J.; Maclellan, K.; Benzerara, K.; Boisset, N. Preservation of protein globules and peptidoglycan in the mineralized cell wall of nitrate-reducing, iron(II)-oxidizing bacteria: A cryo-electron microscopy study. *Geobiology* **2011**, *9*, 459–470.
- (25) Hohmann, C.; Winkler, E.; Morin, G.; Kappler, A. Anaerobic Fe(II)-Oxidizing Bacteria Show As Resistance and Immobilize As during Fe(III) Mineral Precipitation. *Environ. Sci. Technol.* **2010**, *44*, 94–101.
- (26) Rosen, B. P. Biochemistry of arsenic detoxification. *FEBS Lett.* **2002**, *529*, 86–92.
- (27) Stolz, J. F.; Basu, P.; Santini, J. M.; Oremland, R. S.. Arsenic and Selenium in Microbial Metabolism. *Annu. Rev. Microbiol.* **2006**, *60*, 107–130.
- (28) Zouboulis, A. I.; Katsoyiannis, I. A. Recent advances in the bioremediation of arsenic-contaminated groundwaters. *Environ. Int.* **2005**, *31*, 213–219.
- (29) Senn, D. B.; Hemond, H. F. Nitrate controls on iron and arsenic in an urban lake. *Science* **2002**, *296*, 2373–2376.
- (30) Kilcoyne, A. L. D.; Steele, W. F.; Fakra, S.; Hitchcock, P.; Franck, K.; Anderson, E.; Harteneck, B.; Rightor, E. G.; Mitchell, G. E.; Hitchcock, A. P.; Yang, L.; Warwick, T.; Ade, H. Interferometrically controlled scanning transmission microscopes at the Advanced Light Source. *J. Synchrotron Radiat.* **2003**, *10*, 125–136.
- (31) Ditchburn, R. W. *Light*, 2nd ed.; Blackie & Sons: London, 1963; pp 582–585.
- (32) Hitchcock, A. P. aXis2000 written in Interactive Data Language (IDL); 2011; It is available free for non-commercial use from <http://unicorn.mcmaster.ca/aXis2000.html>.
- (33) Chinga, G.; Syverud, K. Quantification of paper mass distributions within local picking areas. *Nord. Pulp Pap. Res. J.* **2007**, *22*, 441–446.
- (34) Walter, T.; Shattuck, D. W.; Baldock, R.; Bastin, M. E.; Carpenter, A. E.; Duce, S.; Ellenberg, J.; Fraser, A.; Hamilton, N.; Pieper, S.; Ragan, M. A.; Schneider, J. E.; Tomancak, P.; Hériché, J.-K. Visualization of image data from cells to organisms. *Nat. Methods* **2010**, *7*, S26–S41.
- (35) Benzerara, K.; Morin, G.; Yoon, T. H.; Miot, J.; Tylliszczak, T.; Casiot, C.; Bruneel, O.; Farges, F.; Brown, G. E. Jr. Nanoscale study of As biomineralization in an acid mine drainage system. *Geochim. Cosmochim. Acta* **2008**, *72*, 3949–3963.
- (36) Tran, N.; Wilson, M.; Milev, A.; Dennis, G.; Kamali Kannangara, G. S. Formation mechanism and surface property of exfoliated silica nano-plates. *J. Phys.: Conf. Ser.* **2008**, *100*, 012013.
- (37) Lawrence, J. R.; Swerhone, G. D. W.; Leppard, G. G.; Araki, T.; Zhang, X.; West, M. M.; Hitchcock, A. P. Scanning transmission X-ray, laser scanning, and transmission electron microscopy mapping of the exopolymeric matrix of microbial biofilms. *Appl. Environ. Microbiol.* **2003**, *69*, 5543–5554.
- (38) Dynes, J. J.; Tylliszczak, T.; Araki, T.; Lawrence, J. R.; Swerhone, G. D. W.; Leppard, G. G.; Hitchcock, A. P. Speciation and quantitative mapping of metal species in microbial biofilms using scanning transmission X-ray microscopy. *Environ. Sci. Technol.* **2006**, *40*, 1556–1565.

(39) Kaulich, B.; Gianoncelli, A.; Beran, A.; Eichert, D.; Kreft, I.; Pongrac, P.; Regvar, M.; Vogel-Mikus, K.; Kiskinova, M. Low-energy X-ray fluorescence microscopy opening new opportunities for bio-related research. *J. R. Soc. Interface* **2009**, *6*, S641–647.

(40) Drouin, D.; Couture, A. R.; Joly, D.; Tasted, X.; Aimez, V.; Gauvin, R. CASINO V2.42—A Fast and Easy-to-use Modeling Tool for Scanning Electron Microscopy and Microanalysis Users. *Scanning* **2007**, *29*, 92–101.

(41) Schaedler, S.; Burkhardt, C.; Hegler, F.; Straub, K. L.; Miot, J.; Benzerara, K.; Kappler, A. Formation of Cell-Iron-Mineral Aggregates by Phototrophic and Nitrate-Reducing Anaerobic Fe(II)-Oxidizing Bacteria. *Geobiology* **2009**, *26*, 93–103.

(42) Pantke, C.; Obst, M.; Benzerara, K.; Morin, G.; Ona-Nguema, G.; Dippon, U.; Kappler, A. Green rust formation during Fe(II) oxidation by the nitrate-reducing *Acidovorax* sp. strain BoFeN1. *Environ. Sci. Technol.* **2012**, *46* (3), 1439–1446.

(43) Dixit, S.; Hering, J. G. Comparison of Arsenic(V) and Arsenic(III) Sorption onto Iron Oxide Minerals: Implications for Arsenic Mobility. *Environ. Sci. Technol.* **2003**, *37*, 4182–4189.

(44) Mikutta, C.; Kretzschmar, R. Spectroscopic Evidence for Ternary Complex Formation between Arsenate and Ferric Iron Complexes of Humic Substances. *Environ. Sci. Technol.* **2011**, *45* (22), 9550–9557.